Control of a Canonical Separated Flow

John Griffin[*], Matias Oyarzun[*]
Florida Center for Advanced Aero-Propulsion (FCAAP)
University of Florida, Gainesville, FL

Louis N. Cattafesta[†]
Florida Center for Advanced Aero-Propulsion (FCAAP)
Florida State University, Tallahassee, FL

Jonathan H. Tu[*], Clarence W. Rowley[‡]
Princeton University, Princeton, NJ

Rajat Mittal[†]
Johns Hopkins University, Baltimore, MD

A stalled airfoil can exhibit up to three natural frequencies associated with the separated flow: that of the shear layer, the separation bubble, and the wake. This work investigates these flow phenomena using a simplified canonical setup and targets their frequencies with zero-net mass-flux (ZNMF) actuation in order to effectively and efficiently reduce the extent of the separation. First, boundary layer separation is created on a flat plate model, devoid of curvature that would otherwise include effects particular to the type of aerodynamic body, by imposing an adverse pressure gradient via a ZNMF suction/blowing boundary condition on the tunnel ceiling. At a chord Reynolds number of 10^5, the nominal two-dimensional characteristics of the flow are verified. The uncontrolled flow is characterized, including identification of the key flow frequency content, prior to strategically targeting this content with unsteady actuation. The identified natural frequencies of the shear layer and wake are then targeted via open-loop ZNMF sinusoidal and burst-modulated (BM) forcing. The results clearly indicate the ability to reattach the separated flow using significantly reduced C_μ values via BM forcing compared to sinusoidal forcing at the actuator resonance frequency.

I. Introduction

Flow separation is one of the most widely studied flow phenomena because of its adverse effects on flow-related devices. The performance losses due to unwanted flow separation are well established (e.g. loss of lift, increased drag, noise generation, structural vibrations, and optical degradation for compressible flows). Many of these conditions of separation have been controlled to mitigate the adverse effects, and all are part of ongoing research. However, effective reattachment or modification of separated flows with minimal control effort is not yet well understood. This is due in large part to the complex, nonlinear nature of fluid mechanics, which results in an overwhelming reliance on open-loop studies that achieve flow control via parametric studies or trial-and-error methods. A better understanding of the natural instabilities of separated flows and their nonlinear interactions is desired.

[*]Graduate Student, Mechanical and Aerospace Engineering, Student Member, AIAA.
[†]Professor, Mechanical Engineering, Associate Fellow, AIAA.
[‡]Professor, Mechanical and Aerospace Engineering, Associate Fellow, AIAA.

The goal herein is to identify and target the natural flow instabilities present in a separated flow and leverage them to either reattach the flow or suppress separation altogether. The experimental platform permits the control of boundary layer separation from a flat plate, on which a strong adverse pressure gradient is imposed via suction/blowing boundary conditions on the ceiling. This platform is ideally suited to this problem because the induced separation exhibits the traditional features of a separated flow while removing any curvature dependence from common lifting-type airfoils. The separated flow is characterized by a shear layer instability, wake vortex shedding, and a potential oscillation associated with the separation bubble.[1,2]

Upon detection of the characteristic frequency content within the baseline flow, a zero-net-mass-flux (ZNMF) actuator is utilized to periodically excite the flow by targeting the natural instabilities. ZNMF actuators, also commonly referred to as synthetic jets, are utilized for this control purpose because of their relatively simple design, ability to use only the working fluid, and flexibility in forcing specific frequency content. In this paper, the effects of varying the forcing frequency and level are measured with the objective of better understanding the interactions of the forcing with the complex dynamics of the baseline flow.

Following this introductory section, more detail is provided for the background of efficient separation control and its unclear dependence on forcing frequency. Then, the experimental setup used to impose and control the boundary layer separation is described in Section III. In the results of Section IV, measurements of the baseline and controlled flows show that an optimal range of forcing frequencies exists, and that this range is dependent upon the characteristic frequencies of the flow. The natural instabilities are leveraged to reattach the flow more efficiently. Concluding comments based on these results are presented along with a future research plan in Section V.

II. Background

Many research studies address optimal forcing parameters for separation control. For unsteady actuation, there are primarily two parameters that are used to characterize the actuation: forcing frequency and actuator output. The former is often represented as a non-dimensional frequency $F^+ = f/f_\mathrm{n}$, where f_n is some natural frequency of the separated flow that can be defined using appropriate length and velocity scales. The latter is traditionally described by the momentum coefficient C_μ, a ratio of momentum output by actuation to the freestream momentum over a reference area of the platform. It is well understood that for sinusoidal forcing, control authority increases monotonically with C_μ.[3,4,5,6] However, control authority varies non-monotonically with F^+.[7,8,9,10] Thereby, a more efficient C_μ may be achieved by leveraging a specific value or range of values for F^+. This is crucial for high-speed flows and other situations that require effective control via actuation limited to low forcing levels.

Unfortunately, there is not a single definition of F^+ because classic stall can be characterized by up to three natural frequencies: that of the separated shear layer, the wake, and, in the event of reattachment, the separation bubble. Each of these scales by a different length associated with the separation and a characteristic speed, although freestream velocity U_∞ is often used for the latter. For studies that define F^+ based on the model chord length, optimal values of F^+ have been reported between 0.55 and 5.5.[11,3,12,13,14,15,16] Other studies that scale F^+ by the length of the separation bubble observe optimal values between 0.75 and 2.0.[17,18,19] Amitay et al.[20] determined that forcing at extremes of $F^+ > 10$ on an unconventional airfoil outperformed configurations with $F^+ < 4$.

Obviously, there is a lack of consensus concerning optimal forcing frequencies, even if the various definitions of F^+ are recognized. An important aspect to these findings is that control authority is governed by both forcing frequency and C_μ, and neither can be neglected. For instance, ZNMF actuators can exhibit substantial differences in output C_μ for small changes in operating F^+. A lack of understanding of the complex interactions among the multiple frequency components and the corresponding values of C_μ may explain some of the spread in the literature. A more thorough treatment of these issues is presented by Mittal et al.[21] This paper recognizes the discrepancies in optimal control and aims to investigate control authority on a canonical separated flow configuration, where both C_μ and F^+ are carefully treated.

III. Experimental setup

The experimental setup is designed to induce boundary layer separation from the upper surface of a flat plate model with a blunt trailing edge. The condition of the separated flow and the boundary condition for

imposing an adverse pressure gradient are used in a companion computational study by Aram et al.[22,1] An adverse pressure gradient is created by accelerating and then decelerating the flow with a zero-net mass-flux suction and blowing boundary condition on the ceiling of the test section above the model. A general schematic of the flow condition is visible in Figure 1. The separated flow on the upper surface of the plate is controlled with zero-net mass-flux (ZNMF) actuators. Particle image velocimetry (PIV), hot-wire anemometry, steady pressure, and unsteady pressure measurements of the separation region and wake are used to diagnose the established baseline separated flow and then evaluate the effectiveness of the open-loop control. More specifically, the key objectives are to identify the characteristic frequencies of the flow and then target those frequencies with unsteady open-loop actuation. The following subsections break down the experimental setup into the model, flow facility, and instrumentation.

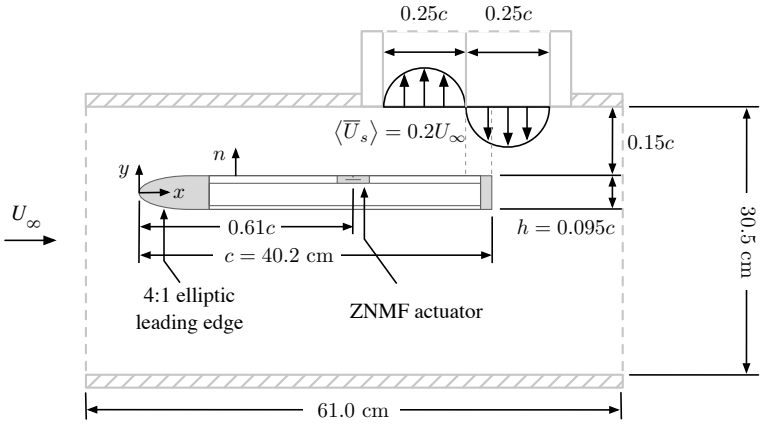

Figure 1. Schematic of the experimental setup.

A. Flat Plate Model

The two-dimensional flat plate model geometry begins with a 4:1 (major axis to minor axis) elliptic leading edge and terminates with a blunt trailing edge. The thickness-to-chord ratio h/c is 9.5% with chord and span lengths of 40.2 cm and 29.2 cm, respectively. The model consists of leading and trailing edge parts, internal support structure, and upper and lower flat plates. The upper plate houses the actuator assembly, six unsteady pressure sensors, and fifteen static pressure ports, all of which are described with more detail in the sections that follow. The trailing edge piece is equipped with fifteen unsteady pressure sensors.

1. Zero-Net Mass Flux Actuator

Control is achieved via a synthetic jet array comprised of four piezoelectric discs (APC Inc., PZT5J, Part Number: P412013T-JB) clamped beneath a rectangular cavity and slot. Disc deflections result in expulsion from and ingestion into the cavity. Over an integer number of cycles, there is no net mass flux caused by the deflection of the discs. The actuator slot is placed at 61% of the model chord length downstream of the leading edge, and this position is dictated by the separation line of the baseline measurements (see Section IV).

The slot width and depth are each 2.0 mm, and its length is 177.8 mm such that the slot covers the central 61% of the overall model span. During experimentation, the actuator slot is covered for the baseline measurements in order to gauge the slot's impact, if any, on the separation characteristics. Otherwise, the slot is open for all measurements. This careful treatment of the slot is necessary to evaluate its passive effect on the separated flow.

2. *Surface Pressure*

Unsteady pressure transducers are used to detect the presence of fluid dynamic structures associated with the induced separation and wake. Flush-mounted Panasonic WM-61A electret microphones (6 mm package diameter) enable real-time measurements of the fluctuating surface pressure. Six sensors, named S1 through S6, are placed in two streamwise rows and flush mounted in the upper flat plate. The two rows symmetrically straddle center span by 2 cm, or roughly 10% chord, in either direction. Their precise placement is given in Figure 2. An additional fifteen sensors are embedded into the trailing edge part, with three placed on the upper surface and the remaining twelve on the base. Among these fifteen sensors, only the five sensors at midspan are used in this paper, and they are denoted by S7 to S11.

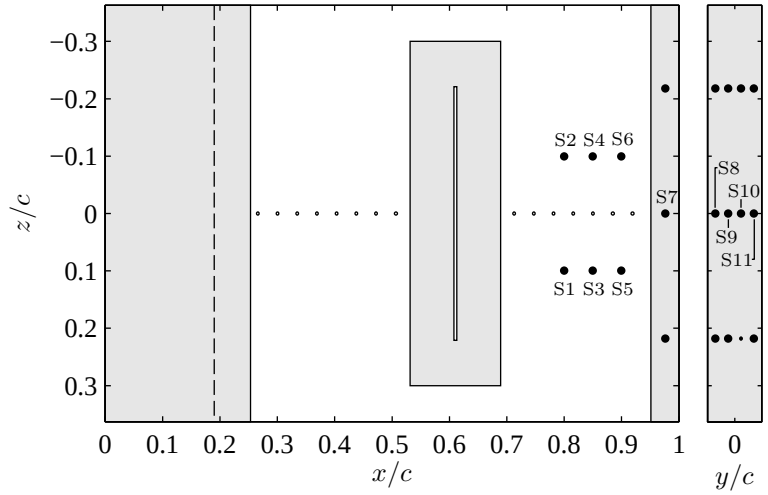

Sensor	x/c	y/c	z/c
S1	0.80	0.048	0.10
S2	0.80	0.048	-0.10
S3	0.85	0.048	0.10
S4	0.85	0.048	-0.10
S5	0.90	0.048	0.10
S6	0.90	0.048	-0.10
S7	0.98	0.048	0.00
S8	1.00	0.034	0.00
S9	1.00	0.011	0.00
S10	1.00	-0.011	0.00
S11	1.00	-0.034	0.00

Figure 2. Unsteady pressure sensor placement on the upper flat plate and flat base. The unsteady sensors used in this study are denoted by their sensor number in the range of S1-S11.

Each microphone is powered by a 4 mA dc current excitation supplied by a National Instruments PXI-1042Q chassis equipped with a NI PXI-4498 data acquisition module. Each channel of this module has 24-bit resolution with 114 dB dynamic range, a built-in anti-aliasing filter, and ac coupling with a 0.5 Hz cut-on frequency. Data are acquired at a rate of 5 kHz.

Steady surface pressure measurements aid in identifying and comparing static pressure distributions experienced by the upper surface for various forcing levels and frequencies. The measurements are made along the center span line of the upper surface flat plate. A total of fifteen static pressure ports, with an inner diameter of 0.711 mm, are installed to measure the static pressure distribution associated with the baseline separation and controlled flows. The distribution of the ports is shown in Figure 2. A 16-channel Esterline Pressure Systems pressure scanner with a range of 10 inH_2O measures the pressure differential between the local static pressure p_s and the freestream static pressure p_∞. For each test case, at least 100 samples is acquired at a rate of 5 Hz.

B. Flow Facility

The entire flow facility consists of two flow-generating devices: a low-speed wind tunnel and an external branch that evacuates airflow through the tunnel's test section ceiling and then returns this flow downstream. Each portion has its own fan, which is operated independently of the other. The external ducting and fan necessary to create the boundary conditions is termed the separation system.

1. *Low-Speed Wind Tunnel*

The experiments are conducted in an Aerolab open circuit, low speed wind tunnel with a test section that measures 30.5 cm × 30.5 cm × 61.0 cm in height, width, and length, respectively. Upstream, the test section is preceded by an aluminum honeycomb panel, two anti-turbulence mesh screens, and a 9:1 contraction section. The airspeed is controlled by a variable frequency driven fan aft of the diffusion section. An external PID

controller sets the test section velocity by referencing the static and stagnation pressures from a Pitot-static tube placed 6.5 cm upstream of the test section inlet, at the mid-height of the test section. The empty test section freestream velocities range from approximately 3 to 45 m/s. The freestream velocity is set to 3.9 m/s, which corresponds to $\mathrm{Re}_c = 10^5$ ($\mathrm{Re}_h = 9.5 \times 10^3$).

2. *Separation System*

The separation system is designed to impose adjacent suction and blowing boundary conditions that create a local adverse pressure gradient. The adverse pressure gradient is imposed to separate the boundary layer on the upper flat surface of the model. The flow enters the separation system through a rectangular cutout in the ceiling. The cutout spans from one sidewall of the test section to the other and is 20.2 cm ($0.50c$) in the streamwise direction. As illustrated in Figure 1, air enters the upstream half of the cutout into the suction portion of the system and returns to the tunnel through the downstream half of the cutout. The time- and spatially-averaged suction velocity is approximately $0.20U_\infty$. Because the extracted air is reinserted, the mass flow rate through the wind tunnel is conserved.

The separation system consists of duct work that encloses the path of the extracted airflow, an in-line duct fan that drives the flow, and internal elements that help condition the flow. A Soler & Palau PV-250x in-line duct fan with a maximum flow rate of 618 CFM drives the flow through the ducting. The rectangular sheet metal ducting is lined with 2.54 cm thick Echo Absorber$^{\mathrm{TM}}$acoustic foam.

Placement of the model relative to the suction and blowing panels is also guided by the simulations, which achieve a closed separation bubble with the trailing edge aligned with the divider plate between the two panels.[1,2] However, the experiments in this paper place the trailing edge of the model $0.050c$ downstream of the divider plate. In addition to this, the transverse placement of the model is set such that the distance between the ceiling and the model's upper surface is $0.15c$.

C. Instrumentation

1. *Hot-wire Anemometer*

The wake frequency is identified with unsteady pressure sensors but also with a hot-wire anemometer. The 5 μm diameter, 1 mm long wire is aligned with the z axis and placed in the wake at a position of $x/c = 1.14$ and $z/c = 0$. Measurements are recorded at three locations: parallel with the upper flat plate surface ($y = h/2$), parallel with the lower surface ($y = -h/2$), and at the central model height ($y = 0$). These measurements are recorded for the baseline flow and the controlled flow cases.

The hotwire is also utilized to characterize the sinusoidal actuator output mean-square velocity in quiescent conditions. The hotwire is aligned with the long dimension of the slot and placed in the middle of the slot. The jet exit speeds are acquired over the center of all four discs for various forcing amplitudes and frequencies for a simple sinusoidal input. Once a single sinusoidal forcing frequency is selected based on the resonant values from each individual disc, the hotwire is traversed in 2 mm increments along the spanwise dimension of the slot. The output speed is measured with all four discs operating at the same frequency and several amplitudes. Once the spanwise variability is assessed, the hotwire is used to measure the actuator output for a burst modulated (BM) input waveform. This time, the hotwire is stationary in the center of the slot, and the response is measured for various modulation frequencies f_m and amplitudes. The carrier frequency f_c of the burst is set to the optimal frequency previously determined from the sinusoidal inputs.

After acquisition of the jet speed $|\mathrm{v}|$ from the actuator, the coefficient of momentum C_μ is computed as

$$C_\mu = \frac{A_\mathrm{s}\mathrm{v}_\mathrm{rms}^2}{A_\mathrm{c}U_\infty^2}, \tag{1}$$

where A_s is the slot exit area, A_c is the cross-sectional area of the model base, and v_rms is the root-mean-square of the jet velocity.

2. *PIV System*

A PIV system is used to acquire both two-component and three-component (stereoscopic) velocity field measurements. A New Wave Research Solo 120-XT Nd:YAG laser coupled with adjustable optics generates a laser light sheet for PIV measurements. All PIV images are captured by LaVision Image Pro X 4M

cameras with 2048×2048 pixel resolution. The laser and cameras are synchronized by a LaVision external programmable timing unit controlled by LaVision DaVis 8.1 image acquisition software. The olive oil particle seeding is produced by a ATI TDA-4B aerosol generator for a typical particle size of 1 μm.

One of the many PIV configurations is for a stereoscopic PIV (SPIV) measurement of the baseline separation region at several spanwise positions. The purpose of this measurement is to assess the spanwise variability of all three velocity components within the separation region. The vertically oriented light sheet is aligned with the midspan line, and then the entire setup is traversed in the spanwise direction to acquire seven evenly spaced SPIV fields between $z/c = [-0.15, 0.15]$. A total of 500 instantaneous spapshots is acquired at each position, except at $z = 0$, where 1000 spanshots are acquired

In addition to this SPIV measurement of the baseline separation region, several different two-component PIV measurements are acquired. These include close-ups of the separation and reattachment locations along the span, a high-resolution view of the separation bubble, and the near wake region directly downstream of the base.

The acquired PIV images are processed with LaVision DaVis 8.1 software. The general image processing steps for all regions include subtracting local average intensities and masking out (ignoring) static portions of the images, i.e. surfaces. Then, multi-grid cross-correlations compute velocity fields, with decreasing interrogation window size for the refining passes. In between passes, outliers are reduced by applying a recursive spatial outlier detection test.[23] The final velocity fields are again tested for outliers, and the detected outliers are removed.[24]

IV. Results and discussion

The results of the experiments described in Section III are discussed below. The discussion of the results is divided into three subsections. First, the baseline separated flow is analyzed using PIV measurements and standard spectral analysis methods from unsteady pressure and hot-wire anemometry. An effort is made to identify key characteristics of the separation bubble and wake, including their dominant frequencies and any coherent structures. Then, the actuator is characterized for a range of input voltages and frequencies. The characterization focuses on burst modulation so that the forcing can target the dominant frequencies of the flow while the actuator operates at one of its resonant frequencies, thereby exciting multiple frequency components. Finally, open-loop control results are presented, including results in which the periodic forcing targets the characteristic flow frequencies. PIV, hot-wire anemometry, and surface pressure are utilized to determine the effectiveness of the control with regards to reattachment.

A. Baseline Flow

The baseline flow is established as the induced separation resulting from the presence of the ceiling boundary conditions. The chord Reynolds number Re_c is defined as

$$\mathrm{Re}_c = \frac{U_\infty c}{\nu}, \tag{2}$$

where ν is the kinematic viscosity, and $\mathrm{Re}_c = 10^5$ for all experiments. This baseline separated flow is distinguished from a traditional bluff-body wake, which results with the removal of the imposed ceiling boundary conditions. The latter case is of interest to the control results because of its attached boundary layers until the abrupt trailing edge corners at the base of the model. However, an important aspect to note is that the two flow conditions are not analogous in a traditional sense. Even in the event of full reattachment of the baseline separated flow on the upper surface, the boundary layer still experiences and recovers from the adverse pressure gradient imposed by the boundary conditions.

With that in mind, the baseline separated flow results follow below. The separation bubble is investigated first by determining the streamwise extent of the separation. Then the three-dimensional characteristics of the mean separation bubble are analyzed using SPIV. Spectral analysis of the unsteady pressure within the separation bubble is performed to determine the frequency content associated with the separated shear layer. The mean flow results from PIV and the dynamical results from unsteady pressure sensors on the base help to characterize the near wake flow. These results are compared to the standard bluff-body wake with the same Re_c.

1. *Separation Bubble – Mean Flow*

The first steps towards characterizing the baseline flow are to verify the existence of boundary layer separation resulting from the imposed adverse pressure gradient and then determine its extent. Two-component PIV is used to accomplish these objectives. Two velocity fields, one zoomed into the suspected separation point and the other zoomed into the suspected downstream reattachment, are measured. In Figures 3a-b, time-averaged streamwise velocity profiles are superimposed on time-averaged streamlines for the two acquired regions. The wall shear stress τ_w, defined as

$$\tau_w = \mu \left. \frac{d\overline{u}}{dy} \right|_{y=0} , \tag{3}$$

is computed from the time-averaged streamwise velocity components near the wall and plotted in Figures 3c-d as the normalized skin friction coefficient,

$$C_f = \frac{\tau_w}{\frac{1}{2}\rho U_\infty^2} . \tag{4}$$

There are 20 velocity measurements within the incoming boundary layer height of approximately 4.8 mm, with the grid point closest to the wall at $n = 0.2$ mm. The figures show that the wall shear stress decreases sharply prior to separation, crosses the $C_f = 0$ line at the point of average separation, and maintains an average flow reversal ($C_f < 0$) until the point of reattachment, where $C_f = 0$ again but with a positive slope that indicates new boundary layer growth. This is confirmed by the average profiles in Figure 3b. The time-averaged separation point x_{sep} and reattachment point x_{att} are determined to be at approximately $0.66c$ and $0.95c$, respectively.

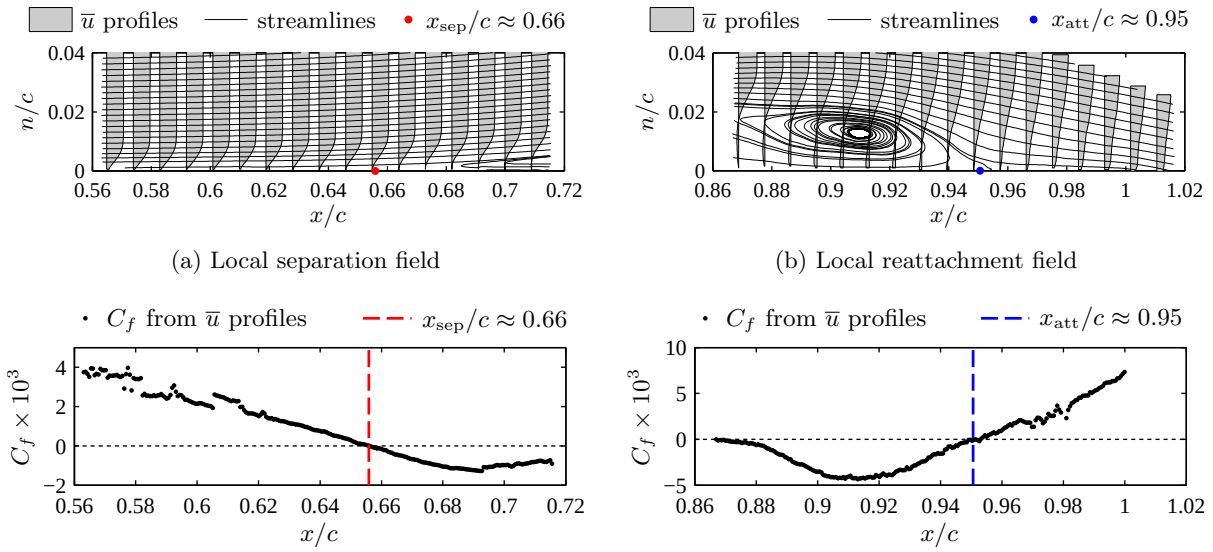

(a) Local separation field

(b) Local reattachment field

(c) Skin friction near separation

(d) Skin friction near reattachment

Figure 3. Time-averaged streamwise velocity profiles are superimposed on average streamlines in the (a) separation and (b) reattachment regions. The zero crossing of their respective skin-friction coefficients determines the average (c) separation and (d) reattachment points. The measurement plane is $z/c = 0.025$.

The average PIV fields shown are from the spanwise position of $z/c = 0.025$ and are computed from a total of 100 instantaneous snapshots. This process is repeated for an additional nine PIV planes between $z/c = 0.22$ and $z/c = -0.22$, with an equal spacing of $\Delta z/c = 0.050$ between neighboring planes. The time averaged separation and reattachment points are calculated for each plane and the results are plotted in Figure 4 as separation and reattachment lines. These measurements are repeated with the actuator slot covered in order to assess the impact of the slot on the time-averaged separated flow topology. The average

lines indicate that there is little difference between the covered slot and the open slot. The average separation and reattachment locations therefore refer to the open slot case hereafter.

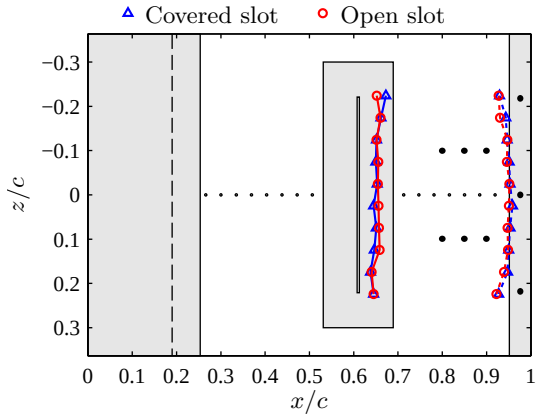

Figure 4. The average separation (solid) and reattachment (dashed) lines are shown relative to model components, including the actuator slot at $x/c = 0.61$, unsteady pressure sensors (larger black circles), and static pressure ports (smaller black circles).

Despite the lack of significant influence from the slot, there are small variations in the extent of the separation bubble along the spanwise direction. At the extremes, near $z/c = \pm 0.2$, reattachment appears to occur slightly further upstream than at the more central span positions. However, the average extent of the separation bubble appears to be uniform within the central range between these two values.

Next, SPIV of the separation bubble is used to more critically assess the magnitude of three-dimensionality within this region. Time-averaged contours of each velocity component are displayed in Figure 5. Concentrating first on the average streamwise velocity, a separation bubble is observed. The streamwise bubble length decreases slightly for the extreme cases of $z/c = \pm 0.15$, which agrees with the previous measurements. The flow upstream and above the separated shear layer is accelerated above the incoming freestream speed before decelerating in the presence of the adverse pressure gradient.

The average transverse velocity component $\overline{v}$ shows reasonable spanwise agreement in both magnitude and distribution. There is a clear upstream and downstream division between positive and negative values for this component. Recall that the dividing plate between the suction and blowing portions of the separation system is located at a streamwise position of $x/c = 0.95$. While the average vertical velocity within the bubble is relatively small, the outer flow rises in the accelerated region before reaching an apex ($\overline{v} = 0$) and changes direction back towards the model surface.

The bounds on the average spanwise contour levels $\overline{w}$ are specifically chosen to match those of the $\overline{v}$ component. The freestream is largely devoid of any significant average spanwise velocity, but pockets exist within the separation region. However, their magnitudes are relatively small, especially within the central span bounded by $z/c = [-0.10, 0.10]$.

2. Separation Bubble – Dynamics

Six unsteady pressure sensors on the upper surface are strategically placed within the separation bubble in order to detect the dynamics associated with the separated shear layer and its development. For the baseline separation, data are acquired at a sampling rate of 5 kHz for 80 seconds. Unsteady pressure spectra are computed using a block size of 1,000 samples, resulting in a 5 Hz bin width. A Hanning window is applied to each data block with 75% overlap. The auto-spectral densities for sensors S1 to S6 are given in Figure 6.

Sensors S1 and S2 are located at $x/c = 0.80$, which is the closest sensor position to the separation point. Though there are several peaks within the spectra of these two sensors, the peaks above 200 Hz have been determined to be acoustics-related to the operation of the tunnel and separation system. Examination of sensors S3 and S4, which are the two sensors at $x/c = 0.85$, reveals a prominent peak at around 90 Hz and increased broadband levels when compared to sensors S1 and S2. Even further downstream, sensors S5 and

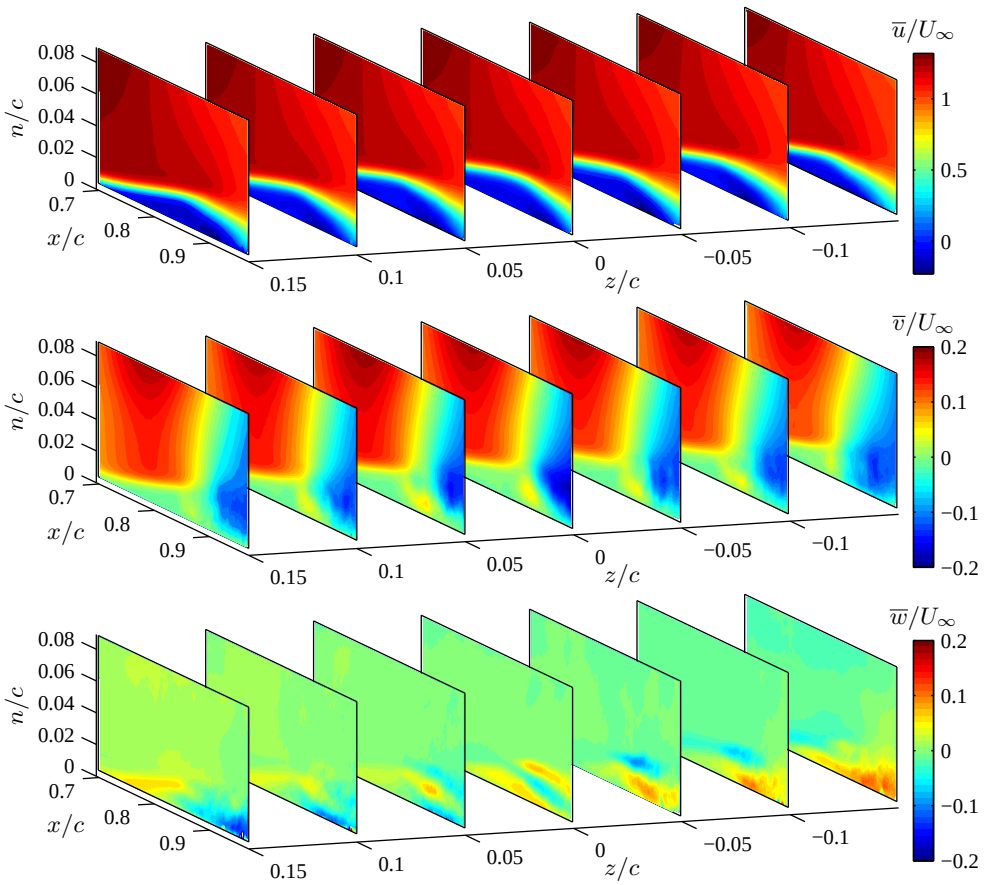

Figure 5. Average streamwise (top), transverse (middle), and spanwise (bottom) velocity components computed from SPIV planes at various slices along the spanwise dimension.

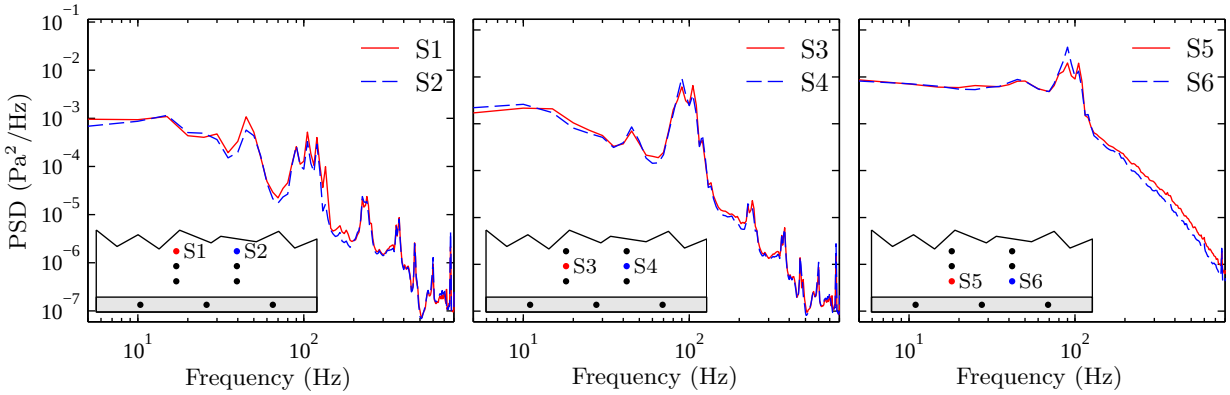

Figure 6. Power spectral densities of unsteady pressure sensors (left) S1 and S2, (center) S3 and S4, and (right) S5 and S6. The sensor locations are marked in the southwest corner of each plot.

S6 at $x/c = 0.90$, have even higher broadband levels but still show the peak frequency at 90 Hz. Due to the placement of these sensors underneath the separated shear layer and the increased turbulence levels observed in the downstream portion of the separation bubble, this 90 Hz is hypothesized to correspond to the shear layer frequency.

This hypothesis is supported by instantaneous velocity fields of the separation region. Figure 7 shows the vorticity of an instantaneous example snapshot. This snapshot provides a useful reference for the locations

of the sensors in Figure 6 (x/c = 0.80, 0.85, and 0.90) relative to the separated shear layer. Downstream from the laminar separation, the Kelvin-Helmholtz instability leads to roll-up of the shear layer. Resulting vortices "pinch" off, convect downstream, and break up into less coherent eddies prior to reaching the trailing edge.

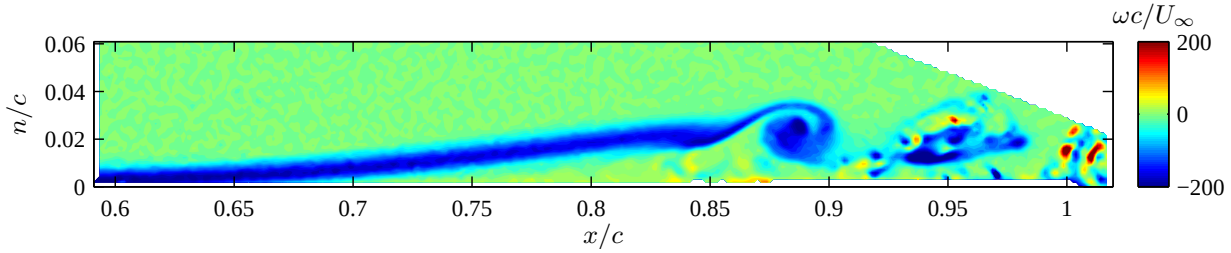

Figure 7. Instantaneous vorticity from a PIV snapshot of the baseline separation region.

Because of this convective instability, cross correlations between sensors along a similar flow path are used to calculate the convective time delay τ_c. The peak in the cross-correlation coefficient ρ corresponds to the average time it takes for coherent structures to convect from one sensor to the next. The cross-correlation coefficients between sensor pair S3 and S5 and also pair S4 and S6 are plotted in Figure 8. The average delay associated with both of these pairings is 8.8×10^{-3} seconds, which amounts to a convection speed of U_c = 2.27 m/s with 2 cm between sensors. From Figure 7, the distance between the two vortex cores is estimated as approximately $0.065c$ (2.6 cm). This convection speed and vortex spacing estimate the frequency of the convecting vortices to be 87 Hz, which agrees well with the observed spectral peak. Therefore, the shear layer frequency f_{SL} is identified as approximately 90 Hz.

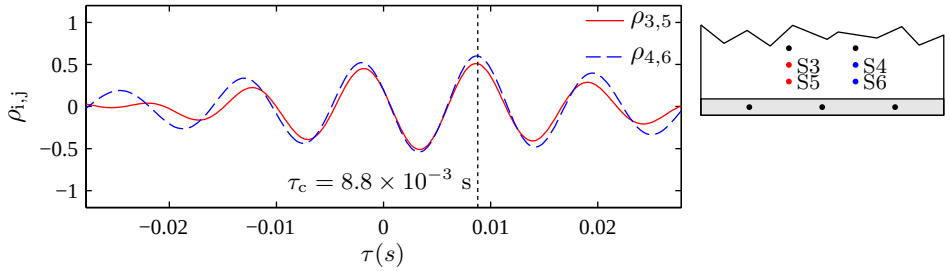

Figure 8. The cross-correlation coefficient between highlighted pressure sensors at equal spanwise but different streamwise positions.

3. Wake – Mean Flow

The next region to investigate for the baseline separated flow is the wake. A natural comparison for this region is the bluff-body wake with Kármán vortex shedding. In additional to the baseline separated flow, measurements are made for this bluff-body wake without induced separation, which is referred to as the standard bluff-body wake.

Two-component PIV measures the flow immediately downstream of the base. The time-averaged vorticity $\overline{\omega}$, normalized by U_∞/c, is plotted in Figure 9 for both the baseline flow and the bluff-body wake. The average vorticity of the baseline separation reveals an asymmetric wake with a much thicker shear layer detaching from the upper surface. The induced separation causes the recirculation region to deflect in the negative y direction. Contrary to this, the standard bluff-body wake is symmetric about $y = 0$, at least in a time-averaged sense.

In order to investigate the magnitude and distribution of fluctuations for each of these flow scenarios, the mean turbulent statistics are computed and shown in Figure 10. Again, the asymmetry of the baseline separated flow is immediately apparent in the fluctuations. Most of the fluctuations, especially in the v

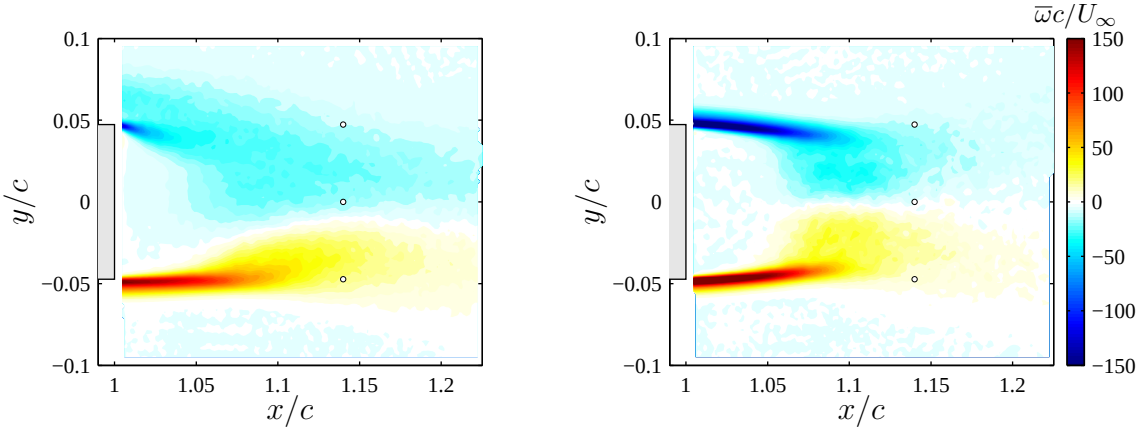

(a) Baseline separated case

(b) Standard bluff-body wake

Figure 9. Average vorticity components computed from PIV of the near wake region at $z/c = 0.025$. Dots indicate the location of hot-wire measurements.

component are prominent in the lower shear layer and much less so in the upper shear layer. The mean turbulence quantities of the standard bluff-body wake, however, exhibit clear symmetry with regions of high fluctuations indicative of Kármán vortex shedding. Finally, the magnitudes of the wake velocity fluctuations in the baseline separated case are nearly half of this in the standard bluff-body wake. This is important when considering the measurement of unsteady pressure fluctuations from the base of the model.

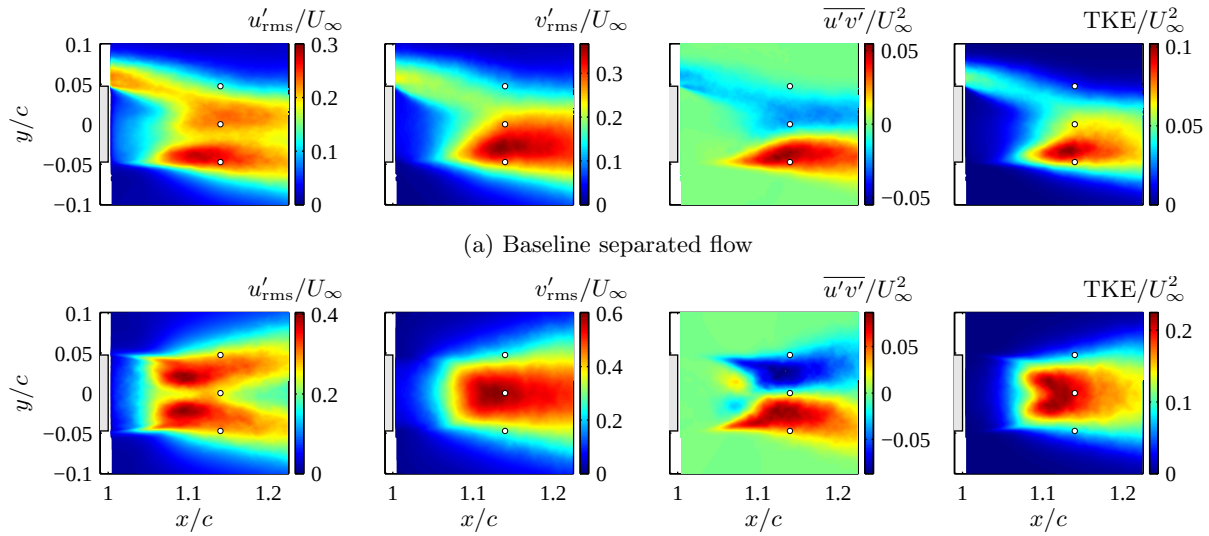

(a) Baseline separated flow

(b) Standard bluff-body wake

Figure 10. Average turbulent quantities computed from PIV of the near wake region at $z/c = 0.025$. Dots indicate the location of hot-wire measurements.

4. Wake Dynamics

The wake dynamics are investigated next in order to identify the characteristic frequency associated with the wake. Four unsteady pressure sensors on the base of the model are sampled at a rate of 5 kHz for 80 seconds. The auto-spectral densities for these sensors are shown in Figure 11. The spectral parameters are data block sizes of 1,000 samples, frequency bin width of 5 Hz, a Hanning window applied to each block,

and 75% overlap.

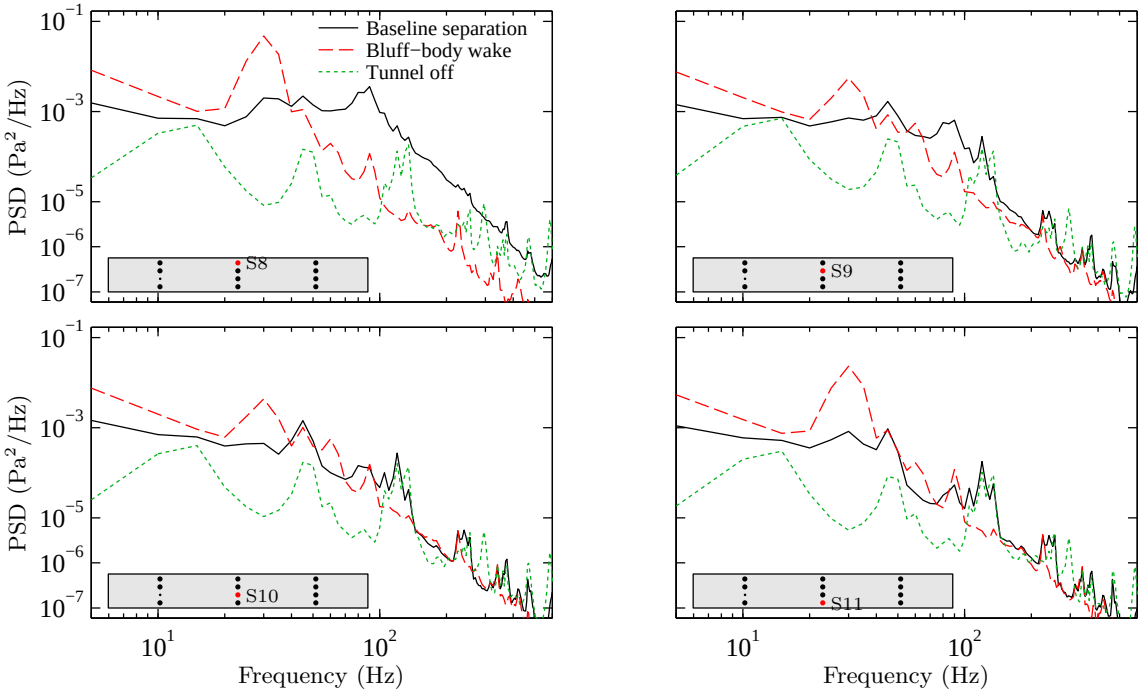

Figure 11. Power spectral densities of unsteady pressure sensors S8 through S11. The sensor locations are marked in the southwest corner of each plot.

The black lines represent the baseline separated flow case. For sensor S8 near the upper surface, the shear layer frequency of 90 Hz persists, but there does not appear to be an additional strong peak associated with any traditional wake-like coherent structures. To verify that these sensors are capable of detecting wake oscillations, the bluff-body wake case is also recorded and shown as the dashed red line. A new peak at approximately 30 Hz appears for all sensors, but the peak magnitude is largest for sensors closest to the upper and lower corners of the base (sensors S8 and S11). When this frequency is normalized, its Strouhal number St_h is 0.25, where

$$\mathrm{St}_h = \frac{fh}{U_\mathrm{W}} \,. \tag{5}$$

The speed $U_\mathrm{W} = 4.5$ m/s is the freestream velocity underneath the model and at the trailing edge.

Referring back to the turbulent statistics for the baseline wake and the bluff-body wake (see Figure 10), the differences in the magnitude and distribution of high-energy fluctuations between these two cases suggests that the vortex shedding for the baseline separated flow is primarily from the lower surface shear layer. The combination of those results with the unsteady pressure spectra suggests that the pressure fluctuations associated with this shedding are not as impactful on the model base and therefore not detected relative to the broadband pressure levels and potential disturbances.

To remedy this, a hotwire is placed downstream of the trailing edge, at a location of $x/c = 1.14$ in order to further investigate the wake dynamics. The hotwire's transverse placement is set to three positions: aligned with the upper model surface ($y/h = 0.5$), aligned with the lower model surface ($y/h = -0.5$), and aligned with the central height of the model base ($y = 0$). These locations are shown as dots in Figures 9-10 and are selected in order to detect velocity fluctuations indicative of vortex shedding from the upper shear layer, the lower shear layer, and potential interaction, respectively.

Auto-spectral densities of the hotwire in the bluff-body wake flow and baseline separated flow are computed and shown in Figure 12. Parameters important to the spectral content include a sampling frequency of 5 kHz, a series duration of 80 seconds, data blocks of 5,000 samples (1 Hz frequency bins), 75% overlap, and application of the Hanning window function. The resulting spectra from the bluff-body wake case clearly show agreement between the dominant peaks associated with the upper and lower shear layers. However,

when the hotwire is placed centrally behind the base of the model, the apparent dominant peak doubles in frequency. This effect is caused by the hotwire's inability to detect velocity direction. The hotwire senses the oscillatory nature of the wake velocity as only positive shifts in speed, which gives rise to a doubling of the primary shedding frequency.

During one cycle of a standard bluff-body wake, the centerline of a wake experiences two vortices, one from the lower shear layer and one from the upper shear layer. At the wake centerline, each vortex produces a velocity deficit in u while also producing a negative minimum or positive maximum in v. Therefore, if the measurements are restricted to u, the spectra would reflect the first harmonic of the shedding frequency. However, because the hotwire does not recognize negative values or flow direction, it is possible that both u and v fluctuations contribute to a perceived frequency doubling of the primary shedding frequency along the centerline. As the probe is moved away from the centerline, both velocity components show the primary shedding frequency and super-harmonics.

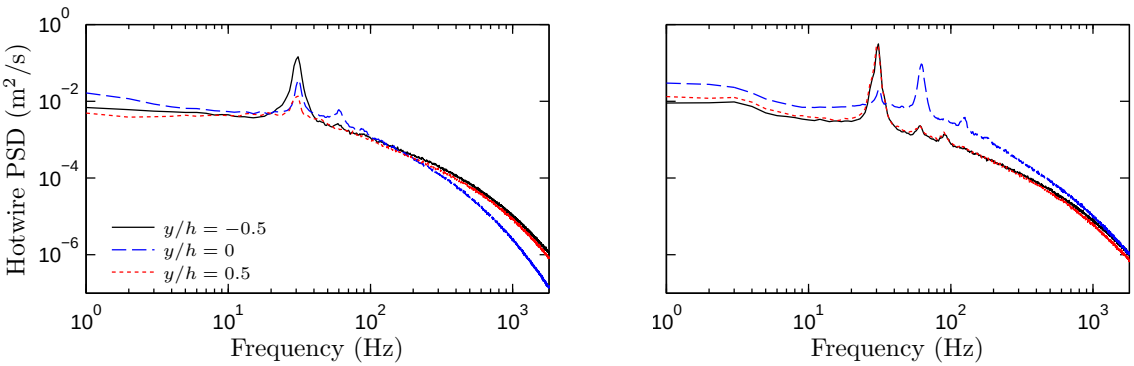

(a) Baseline separated flow

(b) Standard bluff-body wake

Figure 12. PSD of a single probe hotwire placed $0.14c$ downstream of the trailing edge ($x/c = 1.14$).

This spectral analysis is repeated for the wake from the baseline flow. However, the spectra show an overall decrease in the power of the fundamental peak at 31 Hz. This peak's power decreases as the measurement location moves from the lower shear layer towards the upper shear layer. These dynamic results and the full field turbulent statistics suggest that the dominant instability mechanism in the asymmetric wake of the baseline separated flow is vortex shedding from the lower shear layer and that its characteristic frequency f_{w} is 31 Hz.

B. Actuator Characterization

The actuator is initially characterized with a sinusoidal input, and the forcing frequency of 2,050 Hz is determined to be the second resonance frequency of the actuator. This frequency is selected as the carrier frequency of the actuation during control. The output from the actuator is then determined to be uniform across the spanwise direction of the slot, particularly in the span of $z/c = [-0.15, 0.15]$ where $\mathrm{v_{rms}}$ is to within 0.2 m/s of the spanwise average. The burst modulation (BM) waveform type is selected to modulate the carrier sine wave. BM enables the actuation to target specific frequencies while maintaining a high output based on the carrier frequency. Two periods of an example BM waveform are shown in Figure 13 with six carrier cycles and a modulation period of $1/f_{\mathrm{m}}$. An integer number of carrier cycles within a single burst is enforced with the condition that the number of cycles is the minimum amount to ensure a duty cycle of at least 50%.

The actuator output at the center of the slot is measured for modulation frequencies between 0 and 200 Hz in increments of 10 Hz and for amplitudes from 10 to 80 $\mathrm{V_{pp}}$ in increments of 10 $\mathrm{V_{pp}}$. The coefficient of momentum, defined by Eq. 1, is plotted in Figure 14 for the BM actuation. (In the plot, no modulation of the carrier signal is represented by $f_{\mathrm{m}} = 0$.) There is an immediate drop-off in output as BM is enabled, which is attributed primarily to the approximate 50% duty cycle of the modulated waveforms. Another contributing factor is that the transients involved with starting and stopping the actuator in a burst become

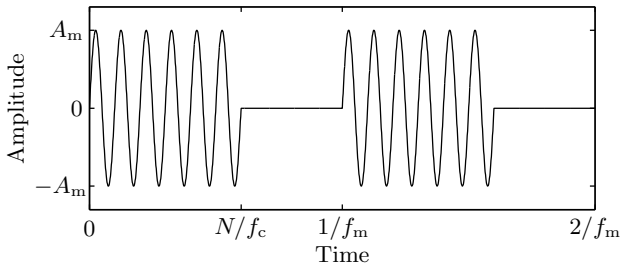

Variable:	Description
f_m:	modulation frequency
f_c:	carrier frequency
N:	number of carrier cycles
A_m:	modulation amplitude

Figure 13. Generic BM waveform with $N = 6$.

a larger portion of the modulation cycle as f_m increases. This is a potential reason for the slightly downward trending output while f_m increases. Control results hereafter use C_μ and f_m when referencing a particular BM control pair.

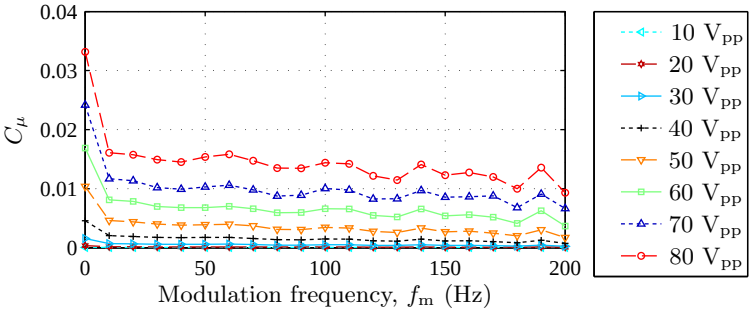

Figure 14. Actuator characterization with various levels and frequencies of BM. The sinusoidal input (no modulation) is included as $f_m = 0$.

C. Open-loop Control

Open-loop experiments sweep through the range of input amplitudes and modulation frequencies given in Figure 14, as well as the no modulation cases referred to as "sine" cases. Surface pressure is measured from the static ports and the unsteady sensors, and the hotwire is placed in the wake at $y = 0$. From these measurements, a select few cases are investigated further with PIV measurements of the separation bubble and wake regions. These results are compared to the data from the baseline separated flow.

1. Controlled Separation Bubble

The initial set of control experiments applies the sinusoidal input waveform (no modulation) at the various C_μ levels provided by the actuator characterization. The static and dynamic surface pressures are measured, and the effectiveness of the control is investigated first without modulation. The coefficient of pressure $C_p = (p_s - p_\infty)/q$ is defined with the dynamic pressure q computed using the freestream speed at the first pressure tap (located at $x/c = 0.27$). These results are shown in Figure 15, where the unsteady pressure is measured by sensor S4. Steady pressure recovery is observed for many of these control cases, and the adverse pressure gradient becomes more gradual over the baseline separation region for increasing values of C_μ. In the unsteady pressure spectra, increasing C_μ leads to increased broadband turbulence until $C_\mu = 0.010$. Further increasing C_μ decreases the broadband levels of sensor S4 until the values of 0.024 and 0.033, for which the 90 Hz shear layer frequency appears to be suppressed. There is also a slight tonal peak near the characteristic wake frequency of 30 Hz for these two control cases.

Next, BM actuation is implemented across a wide range of C_μ values and modulation frequencies. The modulation frequency is varied from 10 to 200 Hz in increments of 10 Hz such that both the characteristic

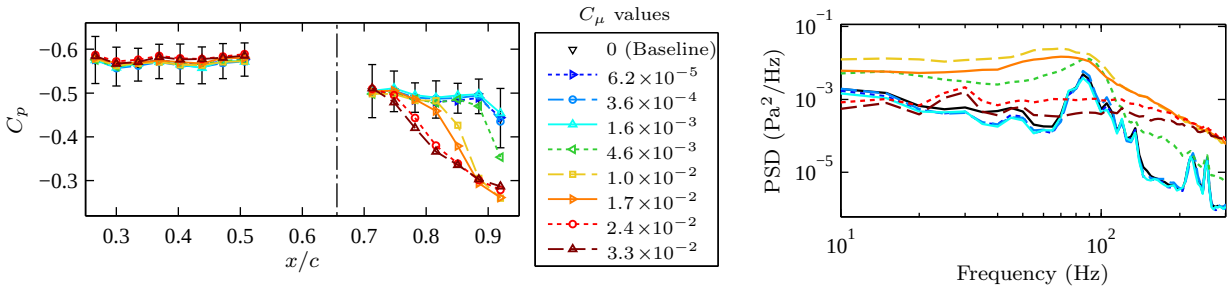

(a) Static pressure

(b) Unsteady pressure

Figure 15. (a) Static pressure along the upper surface of the model and (b) unsteady pressure from sensor S4 with various levels of actuation from a sinusoidal input with $f_c = 2050$. The active control results are compared to the baseline separated flow condition. A vertical *dash-dot* line at $x/c \approx 0.66$ shows the average separation point for the baseline case at $z/c = 0.025$.

shear layer frequency and the characteristic wake frequency are included. From among the 160 total combinations, five interesting cases are selected for further investigation. Because targeting the natural flow frequencies is a focus of this paper, the cases for 30, 90, and 100 Hz are selected for one of the smaller C_μ values that exhibits effective control via C_p distributions and unsteady pressure spectra in the separation region. The range of modulation frequencies near 90 Hz is an optimum in terms of lower levels of C_μ based on pressure recovery in the C_p distributions. Because of this, a case at 90 Hz but with a higher C_μ is added. Finally, the case of sinusoidal forcing and the largest characterized C_μ is included. The C_μ values for these cases are listed in Figures 16 and 17.

The C_p distributions in the separated region aft of the actuator are plotted in Figure 16 for the five selected control cases. From these few, the maximum output case of $C_\mu = 0.033$ and no modulation has the most gradual pressure recovery, which may be indicative of a more reduced or eliminated separation bubble. The remaining cases also show clear pressure recovery but starting at different streamwise distances, which suggests various reattachment points among these cases. The benefit of modulation, however, is more clear when comparing the C_p distributions from the selected cases with C_μ near 1.5×10^{-3} to the sinusoidal input case with $C_\mu = 1.6 \times 10^{-3}$, included in Figure 15a.

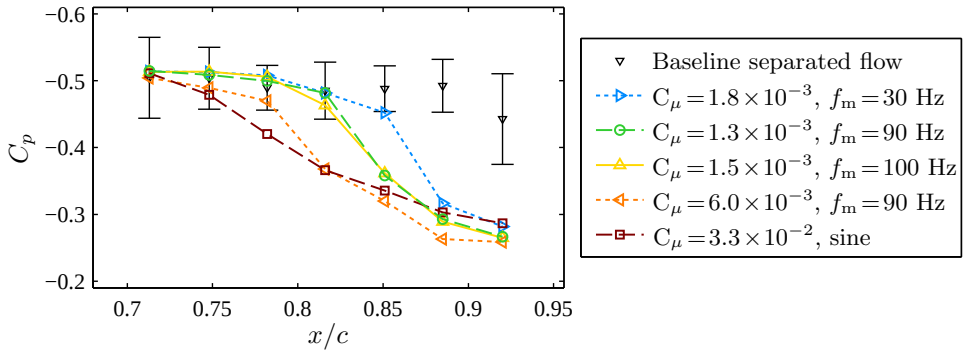

Figure 16. Static pressure along the upper surface of the model with burst modulated actuation at select amplitude and modulation frequency pairings.

PIV data are acquired phase locked at eight equally spaced phases of the modulation cycle for the separation region above the flat plate. The time-averaged u-velocity for the entire modulation cycle is shown in Figure 17 for each of the control cases. The baseline separated flow is also included for comparison. All of the control cases delay separation and promote earlier reattachment but with slightly varying degrees of effectiveness. There does not appear to be a substantial difference in the distribution of u-velocity among

the three lowest C_μ values. The larger modulation frequencies that excite the shear layer frequency achieve a slightly smaller separation bubble. The next highest output case of $C_\mu = 6.0 \times 10^{-3}$ and $f_\mathrm{m} = 90\ Hz$ reduces the average separation bubble size even further. The highest output of $C_\mu = 0.033$ with no modulation appears to suppress separation altogether but at the expense of a 5.5x increase in C_μ. These measurements are consistent with the C_p profiles in Figure 16.

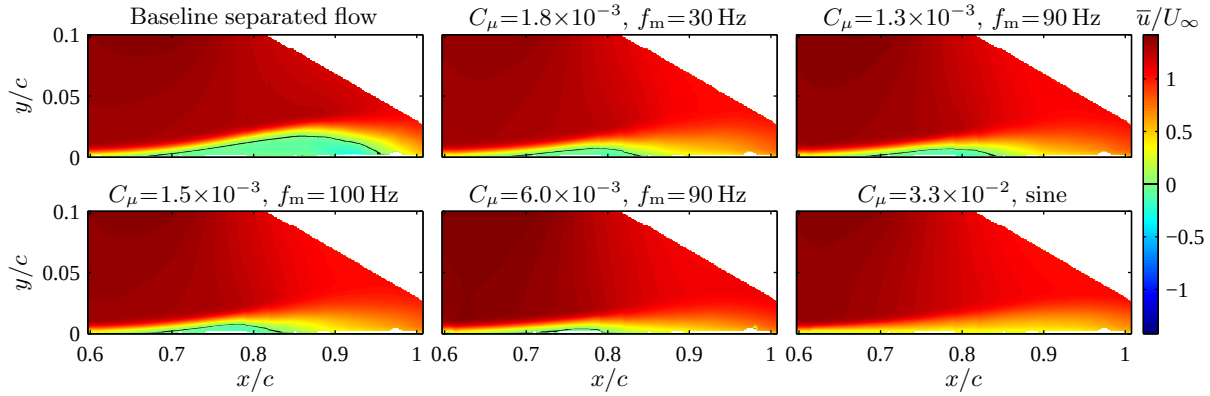

Figure 17. Average steamwise velocity contours of the upper surface separation region for the baseline separated flow and select cases of open-loop control. The vertical axis has been stretched to more clearly visualize the separation.

The dynamics of these results are analyzed by inspection of the phase-averaged velocity fields. Eight equally spaced phase-averaged vorticity contours are plotted in Figure 18 for the three cases with the lowest C_μ values: $C_\mu = 1.8 \times 10^{-3}$ and $f_\mathrm{m} = 30$ Hz, $C_\mu = 1.3 \times 10^{-3}$ and $f_\mathrm{m} = 90$ Hz, and $C_\mu = 1.5 \times 10^{-3}$ and $f_\mathrm{m} = 100$ Hz. The shear layer vortex shedding locks on to the modulation frequency for all three cases. In the phases of the 30 Hz modulation in Figure 18a, successive vortex pairs appear to merge into a larger vortex before detaching and convecting downstream. This causes spacing between convecting vortices to increase because of the decreased rate of formation when compared to the shear layer of the baseline separated flow. However, the average magnitude of the vorticity within the shed vortices is larger than the other cases of similar C_μ. The 90 Hz forcing occurs at or near the natural shedding frequency of the shear layer. This higher rate of vortex roll-up results in tighter spacing between convecting vortices. When this case is compared to the 100 Hz case, the distance between successive vortices is reduced even further because the rate of formation has increased to 100 Hz. The separated shear layer is likely still receptive to this higher burst rate, which enhances mixing of the high-momentum freestream with the low-momentum flow near the surface. The result is a slightly smaller average separation bubble with comparable values of C_μ.

High-amplitude sinusoidal forcing with a C_μ of 0.033 is able to suppress boundary layer separation altogether for this flow. However, a modulated, or pulsed, actuation is able to partially reattach the flow with a much smaller output of $C_\mu = 1.3 \times 10^{-3}$ by targeting the natural shear layer instability. The shear layer locks on to the pulsing, which results in strong, periodic vortex shedding that lowers the separated shear layer, enhances mixing from the freestream into the recirculation region, and reattaches the flow earlier in a time-averaged sense. Because of the shear layer's receptivity to forcing near its characteristic shedding frequency, the actuator output can be reduced by as much as an order of magnitude to yield similar pressure recovery.

2. *Controlled Wake*

The hotwire placed at $y = 0$ and $x/c = 1.14$ is measured during control in order to detect the fluctuations and compare the selected controlled results to the baseline separated flow and the bluff-body wake. Figure 19 confirms that the selected control cases alter the wake dynamics to behave more similarly to the standard bluff-body wake. The agreement of the spectra suggests that the control cases cause the wake flow to resume Kármán-like vortex shedding, though the results at this measurement location do not differ greatly from case to case. The near wake flow does not appear to differ significantly due to the forcing that targets the

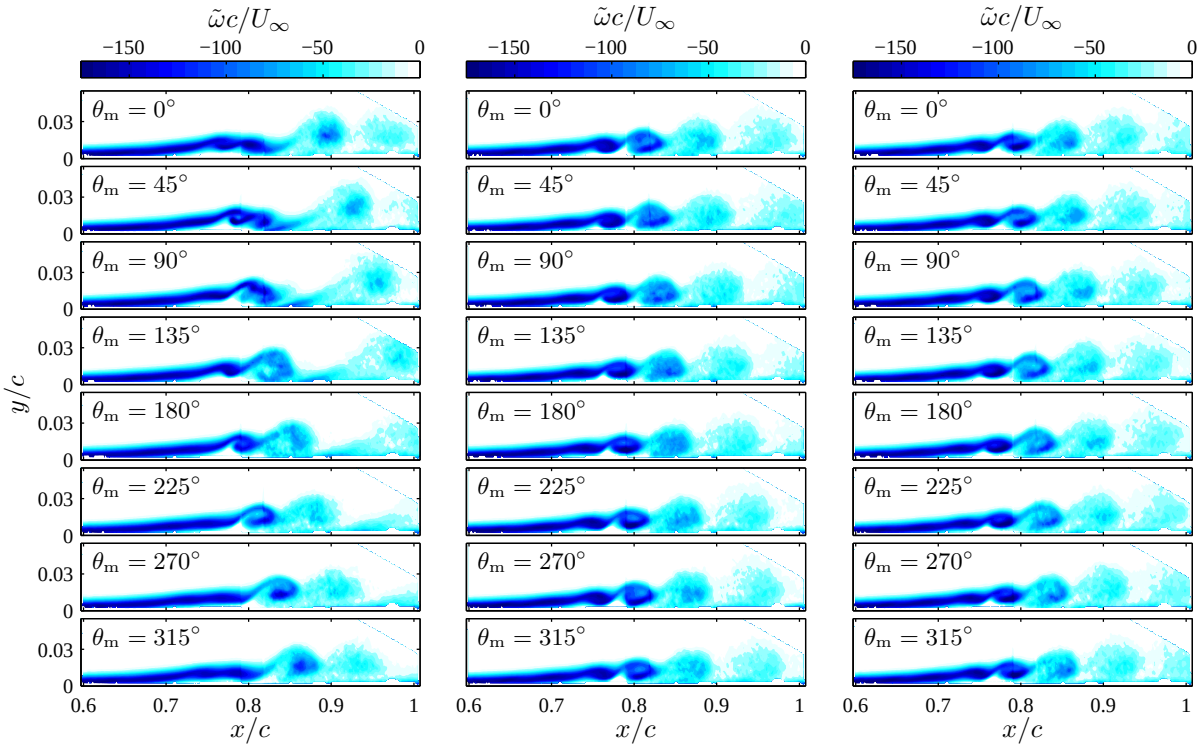

(a) $C_\mu = 1.8 \times 10^{-3}$, $f_m = 30$ Hz (b) $C_\mu = 1.3 \times 10^{-3}$, $f_m = 90$ Hz (c) $C_\mu = 1.5 \times 10^{-3}$, $f_m = 100$ Hz

Figure 18. Phase-averaged vorticity contours of the upper surface separation region with BM control. The vertical axis has been stretched to more clearly visualize the separation.

characteristic wake frequency with $f_m = 30$ Hz. The hot-wire spectrum for this control case does not suggest that the wake's natural shedding is enhanced when compared to the other selected control cases.

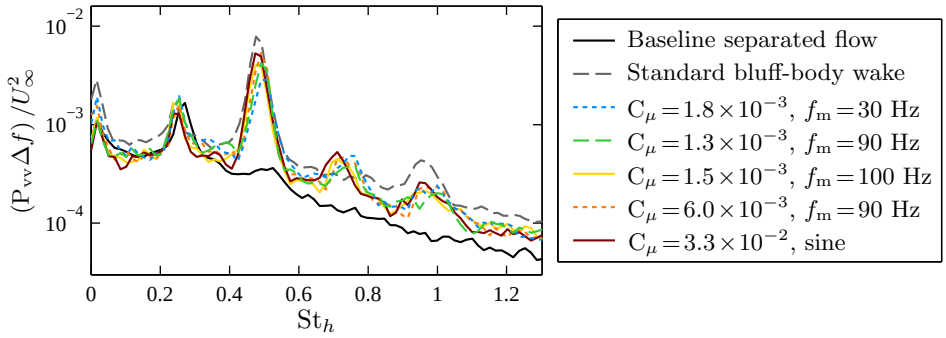

Figure 19. PSD of a hotwire placed in the wake at approximately $x/c = 1.14$ and $y/c = 0$. The active control results are compared to the baseline separated flow and the standard bluff-body wake, both at $Re_c = 10^5$.

PIV is also acquired in the near wake region. For conciseness, the results are restricted to the highest C_μ case with a sinusoidal input. All other cases show similar average and fluctuating flow patterns. Figure 20 shows the average spanwise vorticity for the acquired field. This controlled-flow wake is still asymmetric similar to the baseline separated flow, though to a lesser degree (compare to Figure 9). The significant difference is in the turbulent statistics, shown in Figure 21, where regions of highly fluctuating velocity are more top-bottom symmetric like the standard bluff-body wake. This improved symmetry in velocity fluctu-

ations supports the alternating vortex shedding pattern typical of the standard bluff-body wake (compare to Figure 10), which agrees with the hot-wire results of Figure 19.

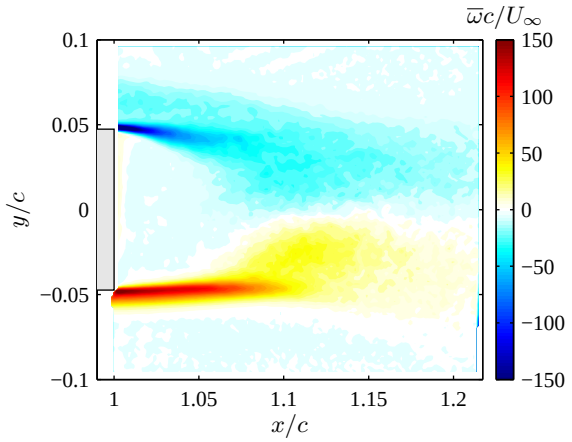

Figure 20. Average spanwise vorticity contour of the near wake region for control with $C_\mu = 0.033$ and no modulation of the sinusoidal input. Measurement plane located at $z/c = 0.025$.

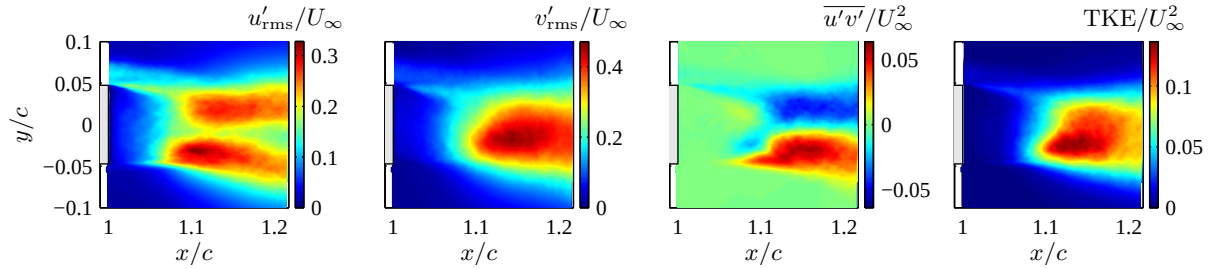

Figure 21. Average turbulent quantities computed from PIV of the near wake region for control with $C_\mu = 0.033$ and no modulation of the sinusoidal input. Measurement plane located at $z/c = 0.025$.

V. Conclusions

In these experiments, the imposed suction and blowing boundary conditions of the proposed canonical configuration are able to induce boundary layer separation from the upper surface of a flat plate model. The separated flow region is investigated, and the time-averaged separation and reattachment points are determined to be nominally two-dimensional across the central spanwise region of the flat plate model. The baseline separated flow causes the wake behind the blunt trailing edge to deflect and exhibit asymmetric velocity fluctuations. The natural frequencies associated with the separated shear layer and the wake are determined from dynamic measurements to be 90 Hz and 30 Hz, respectively.

Unsteady actuation from a ZNMF actuator targets a wide range of frequencies by utilizing a burst modulated input signal. Both the shear layer frequency and wake frequency are targeted via open-loop control. Surface pressure and PIV measurements determine that the burst-modulated flow can reattach with a much smaller C_μ value than is required without modulation of the input sinusoidal waveform. The optimal forcing frequency to achieve pressure recovery given similar values of C_μ coincides with the shear layer frequency from the baseline separated flow, though forcing at the wake frequency is also effective to a lesser extent. This is due to the modulated output's ability to perturb multiple frequency scales, thereby utilizing the flow's natural shear layer instability to more efficiently reattach the separated flow.

Future research plans include investigating the presence of lock-on between the wake and shear layer frequencies. Then, unsteady pressure acquired simultaneously with PIV will estimate the time-resolved

velocity field in a low-order manner.[25,26] This should permit the calculation of DMD modes to identify fixed-frequency flow structures. The results will be be compared to CFD and contribute towards closed-loop control.

Acknowledgements

This work is supported by the Air Force Office of Scientific Research (grant FA9550-09-1-0257), monitored by Dr. Doug Smith, and the Florida Center for Advanced Aero-Propulsion.

References

[1]Aram, E., Mittal, R., Griffin, J., and Cattafesta, L., "Towards Effective ZNMF Jet Based Control of a Canonical Separated Flow," *5th Flow Control Conference*, AIAA, Chicago, IL, 2010.

[2]Tu, J. H., Rowley, C. W., Aram, E., and Mittal, R., "Koopman spectral analysis of separated flow over a finite-thickness flat plate with elliptical leading edge," *49th AIAA Aerospace Sciences Meeting*, No. January, AIAA, Orlando, FL, 2011, pp. 1–14.

[3]Seifert, A., Bachar, T., Koss, D., Shepshelovich, M., and Wygnanski, I., "Oscillatory Blowing: A Tool to Delay Boundary-Layer Separation," *AIAA Journal*, Vol. 31, No. 11, 1993, pp. 2052–2060.

[4]Seifert, A. and Pack, L. G., "Oscillatory Control of Separation at High Reynolds Numbers," *AIAA Journal*, Vol. 37, No. 9, Sept. 1999, pp. 1062–1071.

[5]Glezer, A. and Amitay, M., "Synthetic jets," *Annual Review of Fluid Mechanics*, Vol. 34, No. 1, 2002, pp. 503–529.

[6]Mittal, R. and Rampunggoon, P., "On the virtual aeroshaping effect of synthetic jets," *Physics of Fluids*, Vol. 14, No. 4, 2002, pp. 1533.

[7]Seifert, A. and Pack, L., "Separation Control at Flight Reynolds Numbers: Lessons Learned and Future Directions," *AIAA paper*, Vol. 2542, 2000.

[8]Greenblatt, D. and Wygnanski, I., "Parameters Affecting Dynamic Stall Control by Oscillatory Excitation," *AIAA paper*, Vol. 3121, 1999.

[9]Glezer, A., Amitay, M., and Honohan, A., "Aspects of low-and high-frequency aerodynamic flow control," *AIAA paper*, Vol. 533, 2003.

[10]Raju, R., Mittal, R., and Cattafesta, L., "Towards physics based strategies for separation control over an airfoil using synthetic jets," *AIAA Paper*, Vol. 1421, 2007.

[11]Bar-Sever, A., "Separation control on an airfoil by periodic forcing," *AIAA journal*, Vol. 27, No. 6, 1989, pp. 820–821.

[12]Ravindran, S., "Active control of flow separation over an airfoil," Tech. rep., NASA, 1999.

[13]Wygnanski, I., "Some new observations affecting the control of separation by periodic excitation," *AIAA paper*, Vol. 2314, 2000.

[14]Margalit, S., Greenblatt, D., Seifert, A., and Wygnanski, I., "Active Flow Control of a Delta Wing at High Incidence Using Segmented Piezoelectreic Actuators," *AIAA paper*, Vol. 3270, June 2002.

[15]Darabi, A. and Wygnanski, I., "On the transient process of flow reattachment by external excitation," *AIAA Paper*, Vol. 3163, 2002, pp. 2002.

[16]Funk, R., Parekh, D., Crittenden, T., and Glezer, A., "Transient separation control using pulse combustion actuation," *AIAA Paper*, Vol. 3166, 2002, pp. 2002.

[17]Seifert, A., Darabi, A., and Wyganski, I., "Delay of airfoil stall by periodic excitation," *Journal of Aircraft*, Vol. 33, No. 4, 1996, pp. 691–698.

[18]Pack, L. and Seifert, A., "Dynamics of active separation control at high Reynolds numbers," *AIAA Paper*, Vol. 409, 2000, pp. 2000.

[19]Pack, L., Schaeffler, N., Yao, C., and Seifert, A., "Active control of flow separation from the slat shoulder of a supercritical airfoil," *AIAA paper*, Vol. 3156, No. 1, 2002.

[20]Amitay, M., Smith, D. R., Kibens, V., Parekh, D. E., and Glezer, A., "Aerodynamic flow control over an unconventional airfoil using synthetic jet actuators," *AIAA journal*, Vol. 39, No. 3, 2001, pp. 361–370.

[21]Mittal, R., Kotapati, R. B., and Cattafesta III, L. N., "Numerical study of resonant interactions and flow control," *43rd AIAA Aerospace Sciences Meeting and Exhibit*, AIAA Paper 2005-1261, Reno, Nevada, 2005, pp. 1–12.

[22]Na, Y. and Moin, P., "Direct numerical simulation of a separated turbulent boundary layer," *Journal of Fluid Mechanics*, Vol. 374, No. 1, 1998, pp. 379–405.

[23]Westerweel, J. and Scarano, F., "Universal outlier detection for PIV data," *Experiments in Fluids*, Vol. 39, No. 6, Aug. 2005, pp. 1096–1100.

[24]Griffin, J., Schultz, T., Holman, R., Ukeiley, L. S., and Cattafesta, L. N., "Application of multivariate outlier detection to fluid velocity measurements," *Experiments in Fluids*, Vol. 49, No. 1, April 2010, pp. 305–317.

[25]Tu, J. H., Griffin, J., Hart, A., Rowley, C. W., Cattafesta III, L. N., and Ukeiley, L. S., "Integration of non-time-resolved PIV and time-resolved velocity point sensors for dynamic estimation of velocity fields," *Experiments in Fluids*, Vol. 54, No. 1429, 2013.

[26]Griffin, J., *On the Control of a Canonical Separated Flow*, Ph.D. thesis, University of Florida, 2013.